A 'high-hard' outburst of the black hole X-ray binary GS 1354−64

K. I. I. Koljonen,[1]⋆ D. M. Russell,[1]⋆ J. M. Corral-Santana,[2] M. Armas Padilla,[3,4]
T. Muñoz-Darias,[3,4] F. Lewis,[5,6] M. Coriat[7] and F. E. Bauer[2,8,9]

[1]*New York University Abu Dhabi, PO Box 129188, Abu Dhabi, UAE*
[2]*Instituto de Astrofísica, Facultad de Física, Pontificia Universidad Católica de Chile (IA-PUC), Casilla 306, Santiago 22, Chile*
[3]*Instituto de Astrofísica de Canarias, E-38205 La Laguna, Tenerife, Spain*
[4]*Departamento de astrofísica, Univ. de La Laguna, E-38206 La Laguna, Tenerife, Spain*
[5]*Faulkes Telescope Project, School of Physics & Astronomy, Cardiff University, The Parade, Cardiff CF24 3AA, UK*
[6]*Astrophysics Research Institute, Liverpool John Moores University, 146 Brownlow Hill, Liverpool L3 5RF, UK*
[7]*Institut de Recherche en Astrophysique et Planétologie, 9 Avenue du Colonel Roche, BP 44346, F-31028 Toulouse Cedex 4, France*
[8]*Millennium Institute of Astrophysics (MAS), Nuncio Monseñor Sótero Sanz 100, Providencia, Santiago 7500011, Chile*
[9]*Space Science Institute, 4750 Walnut Street, Suite 205, Boulder, CO 80301, USA*

ABSTRACT

We study in detail the evolution of the 2015 outburst of GS 1354−64 (BW Cir) at optical, UV and X-ray wavelengths using Faulkes Telescope South/Las Cumbres Observatory Global Telescope Network, Small & Moderate Aperture Research Telescope System and *Swift*. The outburst was found to stay in the hard X-ray state, albeit being anomalously luminous with a peak luminosity of $L_X > 0.15 \, L_{Edd}$, which could be the most luminous hard state observed in a black hole X-ray binary. We found that the optical/UV emission is tightly correlated with the X-ray emission, consistent with accretion disc irradiation and/or a jet producing the optical emission. The X-ray spectra can be fitted well with a Comptonization model, and show softening towards the end of the outburst. In addition, we detect a QPO in the X-ray light curves with increasing centroid frequency during the peak and decay periods of the outburst. The long-term optical light curves during quiescence show a statistically significant, slow rise of the source brightness over the 7 years prior to the 2015 outburst. This behaviour as well as the outburst evolution at all wavelengths studied can be explained by the disc instability model with irradiation and disc evaporation/condensation.

Key words: accretion, accretion discs – binaries: close – X-rays: binaries – X-rays: individual: GS 1354−64 – X-rays: stars.

1 INTRODUCTION

Transient low-mass X-ray binaries (LMXBs) produce outbursts reminiscent of dwarf novae, but with intervals of typically several years, higher X-ray luminosities usually approaching the Eddington limit, and decays that can last months (e.g. Chen, Shrader & Livio 1997). They are thought to arise from instabilities occurring in the accretion disc, which result in a sudden increase of mass accretion rate on to the compact object (e.g. Lasota 2001). During an outburst, LMXBs often follow a pattern of X-ray spectral changes resembling each other (e.g. Maccarone & Coppi 2003; Belloni 2010), where the spectra during the rise of the outburst are dominated by a hard, power-law-like spectral component (usually taken to represent the inverse Comptonization of soft seed photons in a plasma cloud of hot electrons), while the spectra during the peak and initial decay of the outburst are dominated by a soft, blackbody-like spectral

component (representing the accretion disc). However, many LMXBs show outbursts that remain in the hard X-ray state for the whole duration of the outburst without changing to the soft X-ray state (Tetarenko et al. 2016, and references therein).

GS 1354−64 (BW Cir) is a dynamically confirmed black hole LMXB, with a black hole mass $>7 \, M_\odot$ in an $\sim$2.5 d long orbit with a low-mass donor star of type G0–5 III (Casares et al. 2004, 2009). The distance to the source is likely greater than 25 kpc and less than 61 kpc (Casares et al. 2004, 2009), but the estimate is heavily dependent on the extinction (lower limit to the distance could be as low as 15 kpc; see Reynolds & Miller 2011). At least two previously confirmed outbursts have been observed from GS 1354−64: in 1987 (Makino 1987; Kitamoto et al. 1990) and 1997 (Brocksopp et al. 2001). The position of GS 1354−64 is also consistent with two earlier outbursts detected from MX 1353−64 (Markert et al. 1977, 1979) and Cen X-2 (Francey 1971). However, it is not clear if these are connected to GS 1354−64 due to large error boxes in the instruments used. The Cen X-2 outburst in 1967 was reported to

⋆E-mail: karri.koljonen@nyu.edu (KIIK); dave.russell@nyu.edu (DMR)

be very bright (∼8 Crab; Brocksopp et al. 2001). However, due to the large distance of GS 1354−64, if Cen X-2 was indeed the same source, the outburst was super-Eddington unless the distance to the source is ∼15 kpc and the mass of the compact object more than 30 M⊙, which seems highly unlikely. The two confirmed outbursts displayed completely different behaviour. In the 1987 outburst, the source transitioned to the soft X-ray state with the accretion disc reaching the innermost stable orbit (Kitamoto et al. 1990). On the other hand, in the 1997 outburst, the source stayed in the hard X-ray state throughout the outburst displaying a pure Comptonization spectrum (Revnivtsev et al. 2000). The outburst profile of the X-ray light curve in the 1997 burst was triangle shaped, and just a single flare was evident, unlike in many other transients that display fast-rise exponential-decay light curves or multiple flares and complicated flare profiles.

The optical magnitudes of GS 1354−64 in late May 2015 were reported to be 1.5–2.0 mag brighter than the quiescent values (Russell & Lewis 2015), and a new outburst start could be noticed in the Monitor of All-sky X-ray Image (MAXI) and Burst Alert Telescope on board *Swift* (*Swift*/BAT) light curves approximately 7 d later as reported in Russell & Lewis (2015), but in retrospect the start of the rise in X-rays can be placed approximately 3–4 d later from the first optical detection. The outburst peaked about 1.5 months later (Koljonen, Russell & Lewis 2015) and the decay lasted about three months.

In this paper, we study the evolution of the 2015 outburst in the optical, ultraviolet (UV) and X-ray frequencies. Multiwavelength observations are important to distinguish different emission scenarios occurring during the outburst. We use the X-ray spectra and light curves from pointing and monitoring observations to constrain the X-ray state and to follow the overall evolution to study whether the source exhibits possible X-ray state changes during the outburst. Several emission processes are likely contributing to the optical/UV bands of LMXBs. The usual candidates are thermal emission from the viscously heated accretion disc (Shakura & Sunyaev 1973; Frank, King & Raine 2002), X-ray irradiation and reprocessing of the outer disc (van Paradijs & McClintock 1994; Dubus et al. 1999) or synchrotron emission from the compact jet (e.g. Hynes et al. 2000; Markoff, Falcke & Fender 2001; Russell et al. 2010, 2013). Also, other emission mechanisms have been suggested: magnetic loop reconnection (e.g. Zurita, Casares & Shahbaz 2003), magnetically dominated compact corona (e.g. Merloni, Di Matteo & Fabian 2000), synchrotron emission from a hot inner accretion flow (Veledina, Poutanen & Vurm 2013) and emission from an advective region (e.g. Shahbaz et al. 2003). In this paper, we use simultaneous optical, UV and X-ray monitoring observations and their correlations to each other, as well as broad-band spectral energy distributions (SEDs), to constrain the optical emission processes.

The structure of the paper is the following. In Section 2, we describe in detail the optical/UV/X-ray observations and how the data were reduced. The outburst characteristics, results from the X-ray spectral and timing analysis, optical/UV/X-ray correlations, broad-band SED and long-term optical light curves are presented in Section 3. We found that the 2015 outburst, similar to the 1997 outburst, stayed in the hard X-ray state, and that the optical and UV fluxes are tightly correlated with the X-ray flux. In addition, we found a statistically significant, gradual rise in the optical brightness during quiescence. In Section 4, we discuss the implications of these results, and in Section 5 we present our conclusions and discuss the ramifications of our results.

2 OBSERVATIONS AND DATA REDUCTION

2.1 Optical/UV observations

2.1.1 Faulkes/LCOGT

Imaging observations of GS 1354−64 were taken with the 2 m Faulkes Telescope South (FTS) situated at Siding Spring, Australia since 2008 January (MJD 54510), as part of a monitoring campaign of ∼40 LMXBs (see Lewis et al. 2008). Here we present more than seven years of monitoring data of GS 1354−64 in quiescence, intense monitoring of the 2015 outburst and monitoring during quiescence post-outburst. During quiescence, observations were typically made once per week when the source was visible, using Bessell *V*, Bessell *R* and Sloan Digital Sky Survey (SDSS) *i*′ filters, with exposure times of 100 s (from 2008 January 10 to 2008 March 24) or 200 s (from 2008 March 31 to 2015) per filter on each date. Once the 2015 outburst was detected, we extended our campaign to make use of the suite of 1 m telescopes on the Las Cumbres Observatory Global Telescope Network (LCOGT) and increased the cadence of our monitoring to ∼3 pointings per week for ∼100 d, adding the Bessell *B*-band filter on four dates. From 2015 June 11 to 2015 September 15, data were acquired from the 1 m telescopes situated at Cerro Tololo (Chile), Siding Spring (Australia) and the South African Astronomical Observatory (SAAO), Sutherland (South Africa) as well as the 2 m FTS. Exposure times were generally either 100 or 200 s per filter during outburst. In addition, a sequence of 15 consecutive *i*′-band images (100 s each) were taken with the 1 m at SAAO on 2015 August 1, to assess the short-term variability properties of the source in outburst. The source was not visible from the ground from mid-September until December. The pixel scale is 0.30 arcsec pixel^{-1} for the 2 m FTS imaging and 0.47 arcsec pixel^{-1} for the cameras on the 1 m network.

Automatic pipelines de-bias and flat-field the science images using calibration files from the beginning and the end of each night. The source is faint in quiescence, and lies in a crowded region of the Galactic plane, and detections of the source depended on the conditions during each night and the quality of the images. Poor seeing, high airmass and dust extinction (especially in the *V* band) were responsible for the source not being detected on all dates. During the quiescent period 2008–2015, secure detections of GS 1354−64 were achieved from 56 images in the *i*′ band, 35 images in the *R* band and 10 in the *V* band. During the 2015 outburst, 51, 37, 35 and 4 detections were made in *i*′, *R*, *V* and *B*, respectively.

We performed aperture photometry using PHOT in IRAF adopting a fixed aperture radius of 6.0 pixels (1.82 arcsec) for the FTS images and 4.5 pixels (2.10 arcsec; different pixel scale) for the 1 m images. These aperture sizes were chosen to ensure that almost all of the flux of the source was inside the aperture, while minimizing the contamination from nearby sources in this crowded field even under poor seeing conditions. The mean seeing is slightly worse for the 1 m network images, and the aperture size in arcsec is therefore slightly larger. For each image in each filter, the same size aperture was used for photometry on two comparison stars in the field with known magnitudes (Brocksopp et al. 2001; Casares et al. 2009) and used for relative photometry to obtain magnitudes of GS 1354−64. Magnitudes of GS 1354−64 were obtained from 228 usable images in total, including a few observations with larger error bars due to bad conditions. Lists of all the observations for all filters can be found in Tables A1–A4.

2.1.2 SMARTS

The 1.3 m SMARTS data were obtained with A Novel Dual Imaging Camera (ANDICAM) using the Bessell *R* filter. The data are automatically bias-subtracted and flat-field calibrated by the SMARTS consortium. The photometry was obtained using two different methods: (i) through point spread function (PSF) fitting using DAOPHOT II/ALLSTAR (Stetson 1987) and (ii) aperture photometry using both DAOPHOT II and the PHOT task in IRAF. In addition, for each aperture photometry, we used two different ways to obtain the final photometry. First, we tried an aperture fixed to 6 pixels (2.21 arcsec) in all images and later we used the optimal aperture for each image following Naylor (1998). However, the most accurate photometry was obtained using the PSF method. Therefore, we decided to continue the analysis with this one. The final PSF model was obtained using an iterative code to select the best fit (i.e. minimum χ^2) among the six different functions available in DAOPHOT II (see Stetson 1987 for further details). To calibrate the field, we selected the five comparisons listed in Casares et al. (2009) and performed differential photometry. The final magnitude of BW Cir is then obtained as the weighted mean of the five individual values for each image. The total number of usable images amounts to 10, with 9 taken during the outburst rise from MJD 57189 to MJD 57211, and one on the decay on MJD 57253. We do not detect any significant deviation in the magnitudes observed with SMARTS compared to those observed with Faulkes/LCOGT based on the outburst evolution in the optical *R* band. However, we do not have strictly simultaneous observations, so direct comparison is not possible. A list of all the observations can be found in Table A5.

2.1.3 Swift/UVOT

In addition, we gathered publicly available pointing observations from the X-ray observatory *Swift* during the whole outburst. In most of the pointings, observations from the UV/Optical Telescope (UVOT) were available in the *U* band. We obtained the source fluxes and magnitudes on the level II pipeline processed image files using UVOTSOURCE, where we used an aperture of 5 arcsec centred on the source. As GS 1354−64 is located in a dense region of the Galactic plane, we select an annulus from 13.3 to 18.5 arcsec for the background region that does not include sources. This ensures also that the diffraction features from nearby bright stars do not contaminate the flux estimates. We select only those pointings where the source is detected at the 5σ level or greater above the background resulting in 31 usable images.

2.1.4 Flux determination

The magnitudes are converted to flux densities using the zero-point for each filter (4137, 3788, 2948, 3631 Jy, for the *B*, *V*-, *R* and *i'* bands, respectively), and dereddened using the Fitzpatrick (1999) parametrization and an extinction coefficient of $A_V = 2.6 \pm 0.31$ (Casares et al. 2004, 2009). This extinction coefficient is measured from the interstellar lines in the optical spectrum. There are no estimates on the Galactic H I column density at the exact location of GS 1354−64. The nearby measurements inside a circle of 1 deg radius vary in a range 5–9×10^{21} cm^{-2} with the nearest value (0.2 deg away) being 6.6×10^{21} cm^{-2} (Kalberla et al. 2005). Using the relation between optical extinction and hydrogen column density (Güver & Özel 2009), these correspond to $A_V = 2.2$–4.3 with the nearest value corresponding to $A_V \sim 3$, which is fairly close to the extinction measured from the interstellar lines. From X-ray

studies of the quiescent X-ray state with *Chandra*, the column density has been estimated as $11 \pm 3 \times 10^{21}$ cm^{-2} (Reynolds et al. 2014). Our mean value of the column density during the outburst is 7.4×10^{21} cm^{-2} (Section 3.2), consistent with the Galactic value. In addition, the extinction coefficient cannot be much larger than 3.5, as it would make the optical/UV SED too steep for any physical process ($\alpha > 3$). Thus, we use $A_V = 2.6$ in the paper.

2.2 X-ray observations

We used X-ray monitoring data from MAXI/GSC (Matsuoka et al. 2009) and *Swift*/BAT (Krimm et al. 2013) and obtained the daily 2–20 and 15–50 keV fluxes from their web interfaces,[1] respectively. In addition, we gathered publicly available *Swift* pointing observations from HEASARC during the whole outburst. The X-Ray Telescope (*Swift*/XRT) windowed timing mode data were processed using XRTPIPELINE in HEASOFT 6.16, and subsequently the source and background spectrum and response files were extracted using XRT-PRODUCTS. Exposure maps were generated separately for each pointing. In addition, we extracted 1.8 ms light curves to be used in a timing analysis. The spectral and timing analysis was undertaken using ISIS (Interactive Spectral Interpretation System; Houck & Denicola 2000) with the SITAR timing analysis module. For spectral fitting, we selected those spectra within MJD 57206–57272 that have exposures $\gtrsim 500$ s. We bin the *Swift*/XRT spectra so that each bin has S/N ≥ 20, and we use the channels with energies from 0.8 to 10 keV. We constructed the power density spectrum (PDS) for each pointing using segments of length 32 768 bins over the whole light curve rejecting the segments with data gaps and averaging over the whole light curve. Subsequently, we fit a simple model to the PDS with ISIS, binning the PDS logarithmically with $\delta f / f = 0.1$. The model includes two zero-frequency Lorentzians, one for modelling the Poisson noise with a deteriorating tail in the higher frequencies because of *Swift*/XRT instrument read-out method and the other for modelling flat top noise in the lower frequencies. In addition, a number of Lorentzians are added to model the QPOs and their harmonics when necessary.
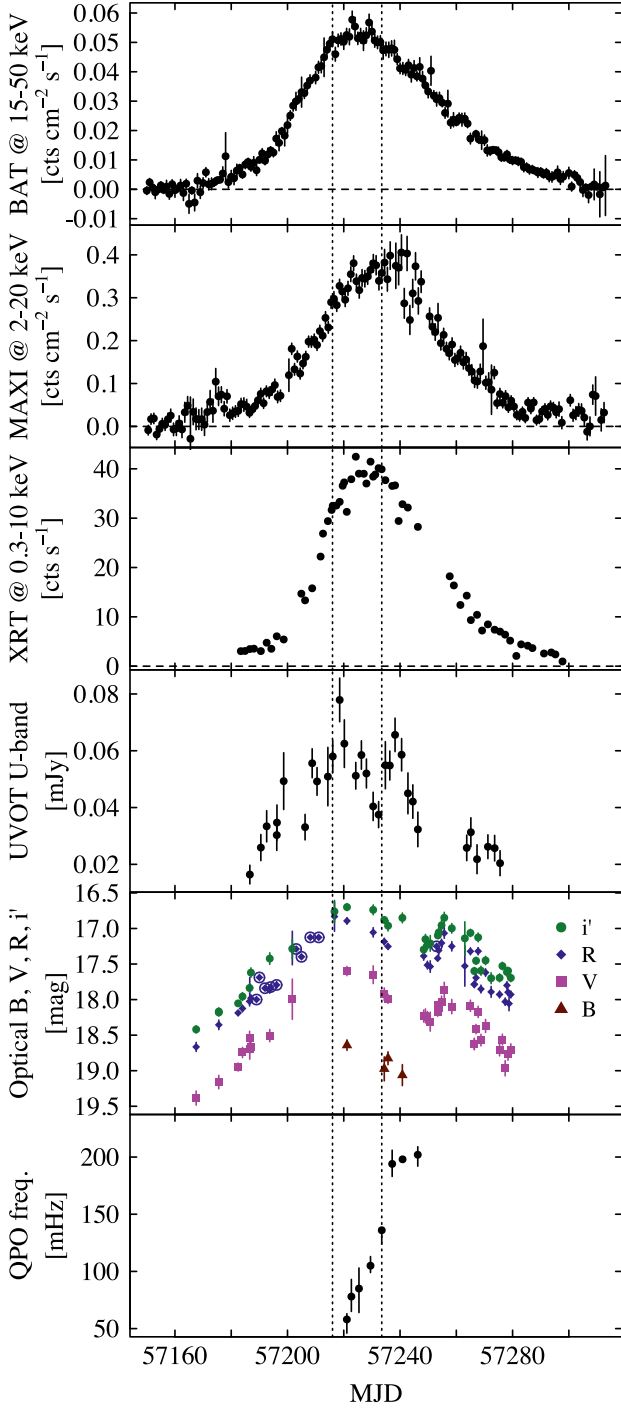
The *Swift*/BAT data were processed using BATBINEVT v1.43 on the survey mode data files (DPH) to first produce sky image files (DPI), which are used to make a masked weighting map for the position of GS 1354−64 with BATMASKWTIMG v1.19. BAT-BINEVT v1.43 is subsequently used to process the DPH files to PHA files using the masked weighting map. A systematic error vector is applied to the spectra to account for residuals in the response matrix using BATPHASYSERR v1.4, and subsequently responses were created with BATDRMGEN v3.4. If more than one spectrum is obtained during a single pointing, these were summed together. For *Swift*/BAT, we use the channels with energies from 15 to 100 keV.

3 RESULTS

3.1 Outburst characteristics

The light curves of the 2015 outburst are plotted in Fig. 1 for X-rays, UV and optical bands. The outburst morphology in hard X-rays is triangular in the nomenclature of Chen et al. (1997) with a flat top. The outburst rise as observed by *Swift*/BAT lasts 46 d

---

[1] MAXI: http://maxi.riken.jp, *Swift*/BAT: http://swift.gsfc.nasa.gov/results/transients/weak/Ginga1354-645/

Figure 1. Monitoring observations of the outburst in X-rays/UV/optical. From top to bottom: *Swift*/BAT 15–50 keV flux, MAXI 2–20 keV flux, *Swift*/XRT 0.3–10.0 keV count rate, UVOT *U*-band flux, optical magnitudes in the *B* (brown triangles), *V* (magenta squares), *R* (dark blue diamonds; SMARTS data are encircled) and *i'* bands (green circles), and QPO centroid frequency from *Swift*/XRT timing analysis. The peak of the outburst as determined from the *Swift*/BAT light curve is delineated with dotted lines.

from MJD 57171 to MJD 57217 and consists of two parts with the flux exponentially increasing with a different e-folding time (see Fig. 2): 13^{+1}_{-2} and 26^{+3}_{-2} d, respectively, with the change taking place on MJD 57202. During the outburst peak that lasts 17 d from MJD 57217 to MJD 57234, the hard X-ray flux is flat with two
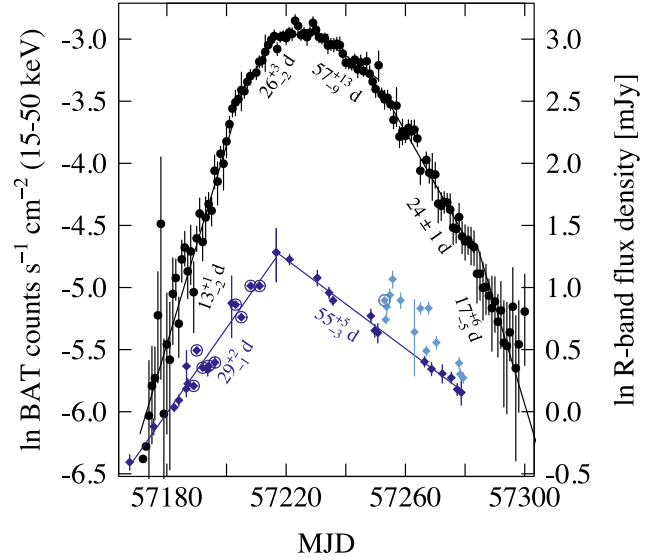
Figure 2. *Swift*/BAT (black circles) and dereddened optical *R*-band (blue diamonds; SMARTS data are encircled) light curves of the outburst over-plotted. In addition, the e-folding times for the exponential rise and decay are marked for both outburst profiles. The light-blue diamonds are excluded in the calculation of the exponential decay in the *R* band.

small flares. The mean *Swift*/BAT flux at the peak is 0.052 ± 0.003 counts cm^{-2} s^{-1}. After the peak, the hard X-ray flux decays with an e-folding time of 57^{+13}_{-9} d until MJD 57251 where it changes to 24 ± 1 d and again to 17^{+6}_{-5} d from MJD 57284 onwards. The soft X-ray light curve is almost identical to the hard X-ray with the outburst peak slightly lagging because of the softening of the X-ray spectra (see Section 3.2). The mean MAXI flux at the peak is 0.34 ± 0.03 counts cm^{-2} s^{-1}. The two X-ray flux regimes are strongly correlated with a Spearman rank correlation coefficient of 0.89 ± 0.01. The outburst, rise and peak durations correspond well to the previous outburst in 1997 (Brocksopp et al. 2001). However, the 2015 outburst is three to four times brighter in the soft X-ray band (2–12 keV) than the outburst in 1997. There are no detectable drops in the *Swift*/BAT light curve; thus, the source does not undergo any state transitions during the outburst.

The optical light curves present similar morphology to the X-rays, and rise and peak in unison with the X-rays indicating correlated behaviour (see Section 3.3). The first detection above the quiescent level in optical wavelengths on MJD 57167 is ∼1.5 mag brighter than the mean quiescent values, and it was observed 3–4 d before a detectable rise in the *Swift*/BAT and MAXI light curves. The optical light curve exhibits similar exponential flux increases as the X-rays, and interestingly the coefficients are closely similar to the X-ray ones near the outburst peak (see Fig. 2) with the e-folding time being 29^{+2}_{-1} d during the rise and 55^{+5}_{-3} d during the decay (we disregard times when the optical is exhibiting reflares). The outburst peak in the optical is sharper compared to the X-ray, except in the *i'* band which shows a flatter profile. The optical magnitudes at the outburst peak are $m_V = 17.60 \pm 0.07$ mag, $m_R = 16.89 \pm 0.05$ mag and $m_{i'} = 16.70 \pm 0.05$ mag. These values are slightly lower when compared to the ones observed in previous outbursts ($m_V \leq 16.9$ in the 1987 outburst and $m_V \leq 17.3$ in the 1997 outburst; Brocksopp et al. 2001) In Fig. 3, we plot the optical SEDs in the rise and decay parts of the outburst. Here, the quasi-simultaneous magnitudes (exposure time and read-out time in between) have been converted to fluxes and dereddened as described in Section 2.1. All the fluxes
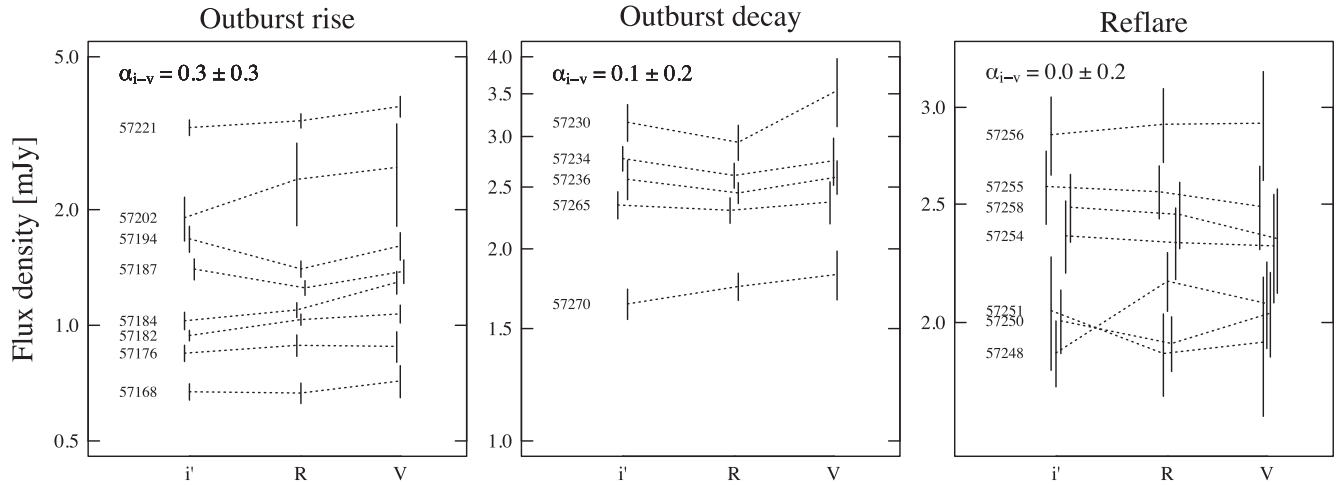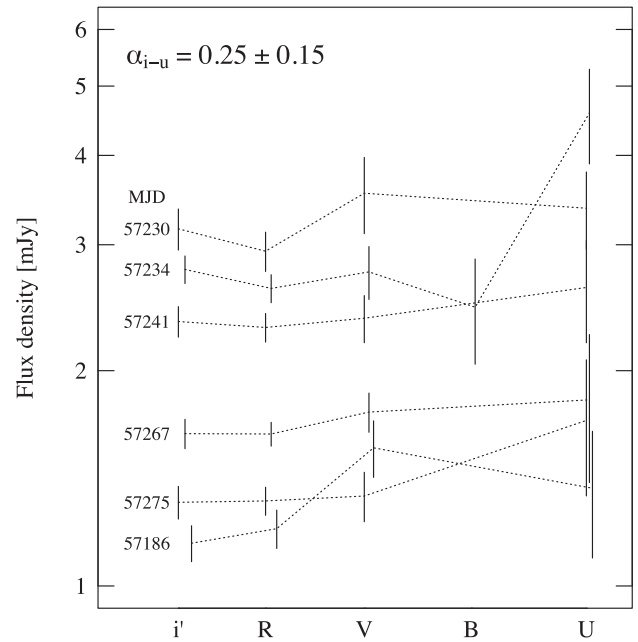
Figure 3. Dereddened optical SEDs for the outburst rise (left), outburst decay (middle) and reflare(s) during decay (right). The subsequent spectra have been shifted vertically for clarity. The average spectral index between the *i'* and *V* band is marked in the upper-left corner of each panel.

are highly correlated and the SEDs are flat with $\alpha = 0.15 \pm 0.30$ ($S_\nu = \nu^\alpha$, or more inverted if using a higher extinction value) during the outburst rise, decay and the optical reflare. During the higher cadence 0.5 h SAAO observation on MJD 57235, the optical fractional rms variability was measured in the *i'* band to be <7 per cent. This is lower than the optical rms of GX 339−4 in the hard state at a similar time resolution (typically ≥10 per cent; Cadolle Bel et al. 2011).

The UV light curve also shows a similar outburst profile as the optical and X-ray. The UV light curve of the outburst rise and decay exhibits similar exponential behaviour as the optical light curves with an e-folding time of ∼30 and ∼56 d during the rise and decay, respectively. The mean flux density during the hard X-ray and optical peak is $F_U \sim 0.06$ mJy, but the UV exhibits moderate flaring in the peak with the flux changing from 0.04 to 0.08 mJy. During the decay there is a strong flare around MJD 57240, but unfortunately there is a gap in optical monitoring during that time apart from a single observation in the *i'* and *B* band. Similarly, the UV light curve has a gap during the optical reflare around MJD 57255, and thus it is difficult to ascertain whether the optical reflare(s) is visible in the *U* band. Fig. 4 shows the optical/UV SEDs when simultaneous (within a day) observations were available. The SEDs are flat up to the *U* band, with the exception of excess in the *V* band during MJD 57187 and in the *U* band during MJD 57234.

3.2 X-ray spectral and timing analysis

All *Swift*/XRT spectra can be fitted with an absorbed power-law model ($\Gamma \sim 1.2$–1.7) excluding a soft excess that seems to originate below 0.8 keV and a collection of emission/absorption lines that are present in some of the spectra, with the most prominent emission line at 2.3 keV (sulphur Kα, mean equivalent width 32 eV), weaker lines around 1.7–1.9 keV probably arising from silicon and 6.4 keV iron Kα line. Adding the *Swift*/BAT spectrum makes the power-law fit worse and a better fit is obtained with a Comptonization model (COMPTT; Titarchuk 1994). Many models were tried in addition to COMPTT, which return similar results. Thus, we fit the individual *Swift* pointings with a model CONSTANT × TBABS × COMPTT, where the constant is allowed for the different calibrations of *Swift*/XRT and *Swift*/BAT. The mean column density is $N_H = 7.4 \times 10^{21}$ cm^{-2}

Figure 4. Dereddened optical/UV SEDs of the outburst when simultaneous (within a day) observations were available. The subsequent spectra have been shifted vertically for clarity. The average spectral index between the *i'* and *U* band is marked in the upper-left corner.

when the absorption is left free in the fits, which is very close to the value obtained from the Galactic H I survey in the field as discussed in Section 2.1. Thus, we fix the absorption to this value. In addition, the electron temperature (kT_e) and the optical depth (τ) are degenerate in the fits; thus, we fix the kT_e to 13 keV (mean value when left free), and fit just the optical depth, and present these as the Compton-*y* parameter: $y = (4kT_e/511) \times \max(\tau, \tau^2)$. During the outburst rise, the error on the lower bound of the disc temperature was found to be pegged to the minimum value; thus, in these cases we fixed the temperature to the upper bound, and proceeded to fit the spectrum again.
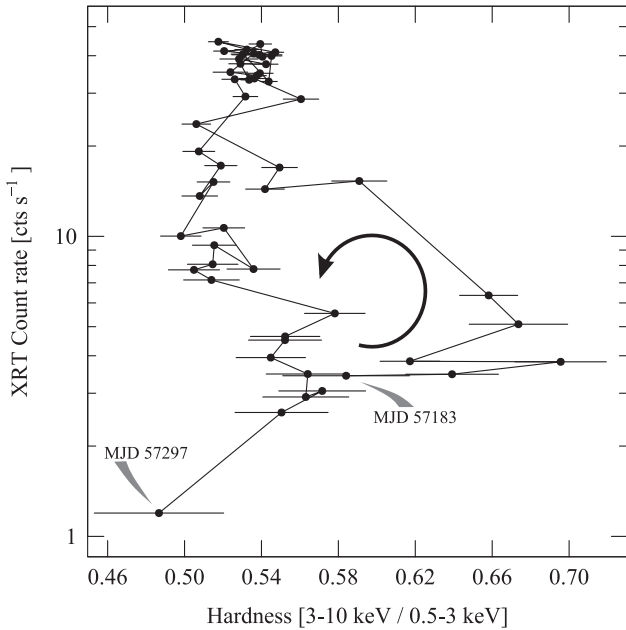
Figure 5. The hardness–intensity diagram of the outburst using *Swift*/XRT pointings. The observation dates for the first and last pointing are marked in the plot, as well as the direction of the evolution of the hardness ratio.

The Compton-*y* changes from ∼1.6 to ∼1.2 indicating spectral softening throughout the outburst. The spectral softening is evident also in the *Swift*/XRT hardness–intensity diagram (Fig. 5), where the outburst rise shows a harder spectrum compared to the outburst decay. As the outburst fades, the hardness ratio returns to values observed at the start of the outburst forming a loop in the diagram. However, as the spectral fits from *Swift* were all fitted well with a Comptonization model and the disc component was not needed, the outburst is hard: the source remained in the hard X-ray state throughout its 2015 outburst, similar to the one in 1997. The mean unabsorbed flux in the X-ray band 0.8–100 keV is 1.03×10^{-8} erg s^{-1} cm^{-2} during MJD 57221–57227, which corresponds to a luminosity of 7.7×10^{38} erg s^{-1} at 25 kpc. We fix the *Swift*/BAT spectra to the level of the *Swift*/XRT spectra in the flux calculation. The parameters and total fluxes of the fits are presented in Table 1 and plotted in Fig. 6. We would like to note that in a few spectra, a satisfactory fit could not be achieved because of prominent emission lines present in the *Swift*/XRT spectra. In these cases, Gaussian profiles were added to the model at the location of the emission lines around 1.7–1.9, 2.3 and/or 6.4 keV.

In some of the *Swift*/XRT PDS, we can identify a low-frequency QPO (in some cases with harmonics, see Fig. 7) that changes in frequency as the outburst evolves. The evolution of the QPO is similar to the outburst in 1997, emerging when the outburst reaches the peak/top part of the light curve, increasing in frequency at the top and settling to an approximately constant value during the decay. In the 1997 outburst, this value corresponded to ∼40 mHz, while in the 2015 outburst the value is five times higher: ∼200 mHz (Fig. 1). The disc temperature is also lower (<0.3 keV) during the outburst rise and settles to a constant value of ∼0.3 keV in the outburst top/decay with two flares approximately on MJD 57230 and MJD 57240. Interestingly, these flares occur roughly at the same time as the UV light curve exhibits flares and thus indicates that the accretion disc, as a source of the seed photons, is also responsible at least in part for the UV emission.

3.3 Optical/UV/X-ray correlation

In Fig. 8, we show the dereddened optical *R*-band flux density as a function of the X-ray fluxes from MAXI, *Swift*/BAT and *Swift*/XRT. The X-ray fluxes are restricted to be within a day of the *R*-band observations. For the outburst rise, there is a clear correlation between the *R*-band and X-ray fluxes with the relation $F_{\text{opt}} \sim F_{\text{X}}^{0.4-0.5}$. At the peak of the outburst, the *R*-band flux density drops slightly faster than the X-ray fluxes, however returning to the same relation during the optical flare and continuing on it as the outburst decays. During a brief period, as the optical reflare rises in magnitude, the *R*-band flux density is anticorrelated with the X-ray fluxes. The optical/X-ray correlations for the *i'* and *V* bands are very similar (see Fig. 12 for the *i'* band including one data point in the quiescent state).

Similar to the optical flux densities, Fig. 9 shows the dereddened *U*-band flux density as a function of the X-ray fluxes, where the X-ray fluxes are restricted to be within a day of the *U*-band observations. As above, the *U* band shows a clear correlation with the X-ray fluxes with the same relation $F_U \sim F_{\text{X}}^{0.4-0.5}$ as the optical. Due to the rather large errors and strong flaring of the *U* band at the peak and decay of the outburst, it is difficult to distinguish whether the *U*-band data exhibit a similar drop as the optical flux densities after the outburst peak. Instead, it is possible that the correlations exhibit two tracks, where the outburst rise is brighter in the *U* band compared to the outburst decay, at a given X-ray flux.

3.4 Multiwavelength SED

The multiwavelength SED from radio to X-rays (around MJD 57190) is plotted in Fig. 10. The observations are not strictly simultaneous: the radio were observed on MJD 57189.32, UV/X-ray on MJD 57190.53, and we took an average of the optical magnitudes observed on MJD 57188.99 and MJD 57190.02 for the *R* band, and on MJD 57187.01 and MJD 57193.69 for the *i'* and *V* bands. The radio spectrum is approximately flat with spectral index $\alpha = -0.10 \pm 0.05$ ($S = \nu^{\alpha}$; Coriat et al. 2015). Similar values were also reported in Brocksopp et al. (2001) for the 1997 outburst: flat or slightly inverted radio spectra were observed during the outburst peak and decay. They could extend the flat radio spectrum to the IR and up to the *R* band. However, the fluxes in the *B* and *V* bands were well above the extended flat radio spectrum and likely corresponded to a thermal disc spectrum. In Fig. 10, we show the possible slopes of a power-law spectrum fitted to the radio data. It seems possible to extend the flat spectrum to optical wavelengths without a cutoff. The *U*-band flux is above the extended radio spectrum by ∼2σ, and appear bluer ($\alpha > 0$), thus likely corresponding to thermal disc spectrum. Overall, the extended radio spectrum does not seem to fully explain the total optical fluxes.

3.5 Long-term optical monitoring

In Fig. 11, we show the complete light curves from optical *i'*, *R* and *V* bands that include the outburst as well as a part of the quiescent state (∼7 years), and a few observations after the outburst. During quiescence, the optical magnitudes vary by a magnitude. The orbital variability is approximately 0.1 mag (Casares et al. 2009), so most of the variability can be attributed to aperiodic flaring activity. We can also identify a statistically significant slow rise in the *i'* and *R* band (not enough data points for the *V* band). We calculate linear least-squares regressions using Monte Carlo bootstrap methods (Curran 2014) from samples that are randomly selected and perturbed according to the data errors. We note the slope and

Table 1. X-ray spectral fits. In the model, the interstellar absorption, N_H, is fixed to 0.74×10^{22} cm^2. The errors are quoted at the 90 per cent confidence level. The columns are (1) the identification number of the pointing, (2) start time of the pointing in MJD, (3) *Swift*/XRT and (4) *Swift*/BAT exposure in seconds, (5) the temperature of the seed blackbody photons, (6) Compton-*y* parameter, (7) model flux in a range 0.8–100 keV, (8) the reduced chi-squared value and (9) the centroid frequency of quasi-periodic oscillation if present.

(1) ObsID[a]	(2) Time (MJD)	(3) XRT exp. (s)	(4) BAT exp. (s)	(5) kT_{bb} (keV)	(6) y	(7) F_X^b	(8) χ^2_{red}/d.o.f	(9) f_{QPO} (Hz)
11	57206.2	945	971	<0.27	$1.42^{+0.13}_{-0.11}$	0.38 ± 0.01	1.22/63	–
12	57208.8	964	990	<0.21	$1.58^{+0.12}_{-0.11}$	0.50 ± 0.01	1.08/69	–
14	57211.8	981	956	<0.18	$1.34^{+0.07}_{-0.08}$	0.56 ± 0.01	1.05/81	–
15	57212.6	591	609	<0.23	$1.64^{+0.13}_{-0.11}$	0.93 ± 0.02	1.04/72	–
18	57215.7	650	667	$0.25^{+0.02}_{-0.02}$	$1.36^{+0.10}_{-0.09}$	0.81 ± 0.02	0.78/81	–
19	57216.1	827	836	<0.14	$1.47^{+0.07}_{-0.07}$	0.88 ± 0.02	1.26/96	–
20	57217.4	1582	1600	<0.12	$1.44^{+0.05}_{-0.05}$	0.87 ± 0.01	1.32/146	–
21	57218.5	449	465	<0.22	$1.29^{+0.09}_{-0.08}$	0.82 ± 0.02	0.98/70	–
22	57219.6	1421	1437	$0.23^{+0.01}_{-0.02}$	$1.40^{+0.06}_{-0.06}$	0.93 ± 0.02	1.23/145	–
23	57220.1	854	870	$0.19^{+0.03}_{-0.03}$	$1.38^{+0.06}_{-0.07}$	0.95 ± 0.03	0.98/103	–
24	57221.1	2086	2110	$0.23^{+0.02}_{-0.01}$	$1.39^{+0.05}_{-0.05}$	1.12 ± 0.02	1.45/169	$0.058^{+0.005}_{-0.012}$
25	57222.7	1175	1124	<0.22	$1.47^{+0.06}_{-0.06}$	1.12 ± 0.01	1.73/123	$0.078^{+0.015}_{-0.013}$
26	57224.3	1075	1090	$0.29^{+0.01}_{-0.02}$	$1.29^{+0.07}_{-0.07}$	0.99 ± 0.02	1.40/128	–
27	57225.4	1828	1834	$0.31^{+0.01}_{-0.01}$	$1.36^{+0.07}_{-0.06}$	1.03 ± 0.01	1.03/177	$0.085^{+0.018}_{-0.021}$
28	57227.1	1085	1098	$0.31^{+0.01}_{-0.01}$	$1.28^{+0.08}_{-0.07}$	0.94 ± 0.02	1.39/122	–
29	57228.0^c	1145	1158	$0.36^{+0.01}_{-0.01}$	$1.43^{+0.11}_{-0.10}$	1.07 ± 0.02	1.63/122	–
30	57229.5	954	981	$0.32^{+0.08}_{-0.01}$	$1.34^{+0.08}_{-0.08}$	1.03 ± 0.02	1.13/117	$0.105^{+0.008}_{-0.006}$
31	57230.4	897	921	$0.28^{+0.02}_{-0.01}$	$1.39^{+0.09}_{-0.08}$	1.03 ± 0.02	1.16/112	$0.105^{+0.008}_{-0.006}$
33	57232.4	998	1024	$0.30^{+0.01}_{-0.01}$	$1.26^{+0.08}_{-0.07}$	0.97 ± 0.02	1.39/120	–
34	57233.5	831	860	$0.30^{+0.01}_{-0.01}$	$1.33^{+0.09}_{-0.09}$	0.98 ± 0.02	1.28/106	$0.136^{+0.000}_{-0.012}$
37	57237.2	887	911	$0.29^{+0.02}_{-0.01}$	$1.40^{+0.10}_{-0.08}$	1.07 ± 0.02	1.55/107	$0.194^{+0.012}_{-0.011}$
38	57238.2	910	923	$0.31^{+0.01}_{-0.02}$	$1.29^{+0.09}_{-0.08}$	0.91 ± 0.02	1.24/109	–
39	57239.5	972	951	$0.34^{+0.01}_{-0.02}$	$1.33^{+0.10}_{-0.10}$	1.16 ± 0.03	1.50/98	–
41	57240.9^c	2152	2177	$0.35^{+0.01}_{-0.01}$	$1.49^{+0.09}_{-0.09}$	0.94 ± 0.02	1.63/168	$0.198^{+0.001}_{-0.001}$
42	57242.8	850	879	$0.29^{+0.01}_{-0.01}$	$1.26^{+0.08}_{-0.09}$	0.76 ± 0.02	1.36/95	–
44	57246.3^c	1058	1082	$0.31^{+0.02}_{-0.01}$	$1.43^{+0.12}_{-0.11}$	0.79 ± 0.02	1.27/96	$0.202^{+0.007}_{-0.010}$
46	57259.1	1045	1062	$0.28^{+0.02}_{-0.02}$	$1.26^{+0.11}_{-0.10}$	0.44 ± 0.01	1.29/74	–
47	57261.4	1104	1133	$0.29^{+0.01}_{-0.03}$	$1.14^{+0.11}_{-0.10}$	0.29 ± 0.01	1.38/65	–
48	57263.7	1187	1191	$0.30^{+0.01}_{-0.02}$	$1.25^{+0.12}_{-0.11}$	0.33 ± 0.01	1.31/72	–
49	57265.2	1077	1099	$0.31^{+0.02}_{-0.02}$	$1.10^{+0.14}_{-0.13}$	0.52 ± 0.02	1.10/57	–
50	57267.4	1004	1015	$0.31^{+0.02}_{-0.03}$	$1.25^{+0.17}_{-0.16}$	0.25 ± 0.01	0.94/57	–
51	57269.2	917	937	$0.28^{+0.04}_{-0.05}$	$1.41^{+0.22}_{-0.20}$	0.23 ± 0.01	1.34/49	–
52	57271.2	1091	1110	$0.27^{+0.02}_{-0.04}$	$1.28^{+0.15}_{-0.15}$	0.21 ± 0.01	1.10/55	–

Notes. ^{a}000338110**
^{b}Units are in 10^{-8} erg s^{-1} cm^{-2}.
^{c}Gaussian profiles added to the model at 1.7–1.9, 2.3 and/or 6.4 keV.

intercept of each fit, and produce 95, 99 and 99.9 per cent limits on the possible regressions (shaded, coloured regions in Fig. 11). We also note the percentage of cases where the slope is 0 or negative, and calculate the significance of a positive slope, which in both cases is $>5\sigma$.

In addition, we include a quiescent data point to the optical/X-ray correlation (Fig. 12) based on *Chandra* observation (Reynolds & Miller 2011) that took place on MJD 55470. There are no simultaneous optical observations during the *Chandra* observation, so we estimate the optical *i'*-band magnitude using the above-mentioned linear least-squares regression to the quiescent data with an error based on the standard deviation of all quiescent data points, and assuming that the stellar contribution can be as high as 50 per cent

(Casares et al. 2004, 2009). It seems that the $F_{i'} \sim F_X^{0.44}$ relation does not continue to the quiescent state and a break between the outburst and quiescent state is evident ($>3\sigma$ away from the best-fitting line). This suggests that the viscously heated disc with a shallower relation ($F_{opt} \sim F_X^{0.3}$; Russell et al. 2006) may dominate the optical emission, rather than X-ray reprocessing, at this low X-ray luminosity.

4 DISCUSSION

Many LMXBs show hard, or 'failed', outbursts, where the source spectral state does not change to the soft state (Tetarenko et al. 2016). These sources differ in orbital periods to each other, and thus sizes of
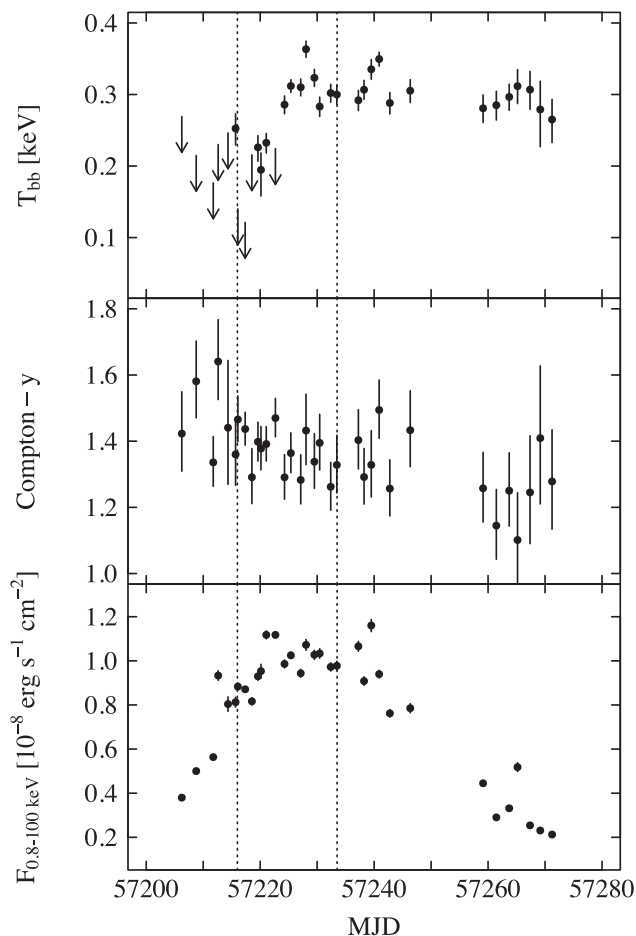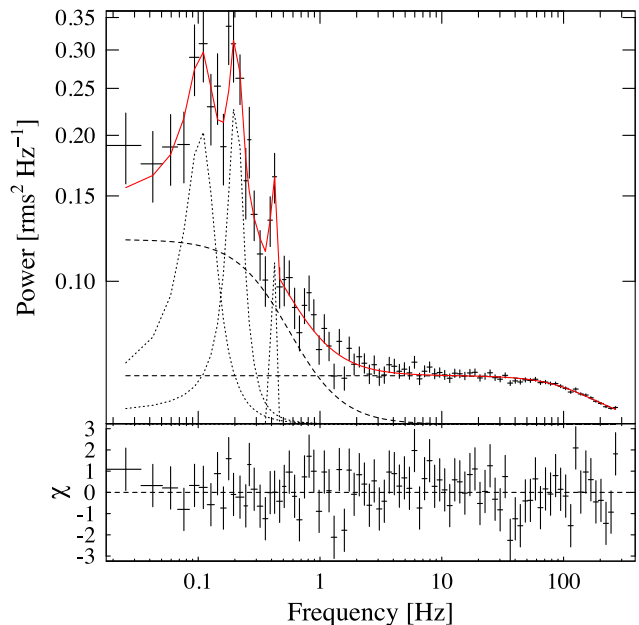
Figure 6. Model parameter evolution throughout the outburst. From top to bottom: the temperature of the seed blackbody photons, Compton-*y* parameter and the model flux in the energy range 0.8–100 keV. The dotted lines delineate the outburst peak as shown in Fig. 1.

Figure 7. PDS (upper panel) from *Swift*/XRT light curve of pointing 00033811041 showing a QPO at 0.2 Hz with a lower and higher harmonic (dotted lines). Red solid line shows the best-fitting model, dashed lines the noise components, and the model residuals are shown in the lower panel.

the accretion discs, which leads to different amounts of accumulated matter in the disc. In addition, these sources present very different light-curve morphologies (Brocksopp, Bandyopadhyay & Fender 2004). The 2015 outburst of GS 1453−64 seems to be a relatively 'clean' outburst, with no secondary maxima (with the exception of optical flares), and all frequencies above optical seem to be correlated with each other. The 2015 outburst has been so far the best covered outburst of GS 1354−64 throughout the electromagnetic spectrum, which gives us another well-sampled data set for the hard outbursts detected from X-ray transients.

4.1 Evolution of the outburst

Accretion discs in LMXBs are strongly irradiated by the X-ray emission of the accretion flow. We discuss below (Section 4.3) that the optical emission is likely partly produced by the reprocessing of the X-ray emission. The irradiation affects the disc properties during the outburst. According to the disc instability model (DIM; e.g. Lasota 2001), during quiescence the accretion disc is replenished, increasing steadily in temperature, until some annulus becomes thermally unstable allowing for ionization of hydrogen. The ionization in turn increases the viscosity of the disc via a magnetorotational instability (Balbus & Hawley 1991), which increases the mass ac-

cretion rate through the disc. This leads to an outburst, where a heating front moves inwards and/or outwards to smaller/larger radii, increasing the mass accretion rate, that increases the X-ray radiation and reprocessing, which in turn helps the heating front propagate further out. In the case of an 'inside-out' burst, the heating fronts propagate slowly to larger radii resulting in slow rise times and symmetric outburst profiles. When the heating front arrives to the outer disc rim, there is a surface density and accretion rate excess that starts to diffuse inwards until the accretion rate is roughly constant in the whole disc. The accretion rate increases by a factor of 3 during this phase.

The behaviour of GS 1354−64 outburst in 1997 as well as the current outburst fits well with the above-mentioned 'inside-out' burst. The increase in the mass accretion rate after the heating front has arrived to the outer disc could be seen in the increasing temperature of the disc, and the increasing frequency of the mHz QPO from 50 to 200 mHz, corresponding to the Keplerian radii of $\log (r/r_g) =$ 4.3–4.1 (or 3×10^{10}–2×10^{10} cm) for a black hole of 10 $M_\odot$, assuming that the origin of the QPOs is geometrical and related to disc truncation. This radius could correspond to the location where the disc changes from an optically thick, geometrically thin disc to an optically thin, geometrically thick disc (e.g. ADAF/RIAF; Yuan, Quataert & Narayan 2003). In the 1997 outburst of GS 1354−64 as well as in other sources, e.g. GRO J1719−24 and XTE J1118+480 (Brocksopp et al. 2004), the evolution of the QPO is similar to the centroid frequency increasing during the peak/decay of the outburst. In the 2015 outburst, the QPO frequency is about five times higher than in the 1997 outburst. At the same time, the soft X-ray luminosity is also several times brighter when compared to the 1997 outburst. This is in line with the truncated disc scenario where the accretion disc approaches closer to the black hole, increasing the QPO frequency and emitting more radiation in the X-ray regime, thus providing more seed photons for the Comptonization and
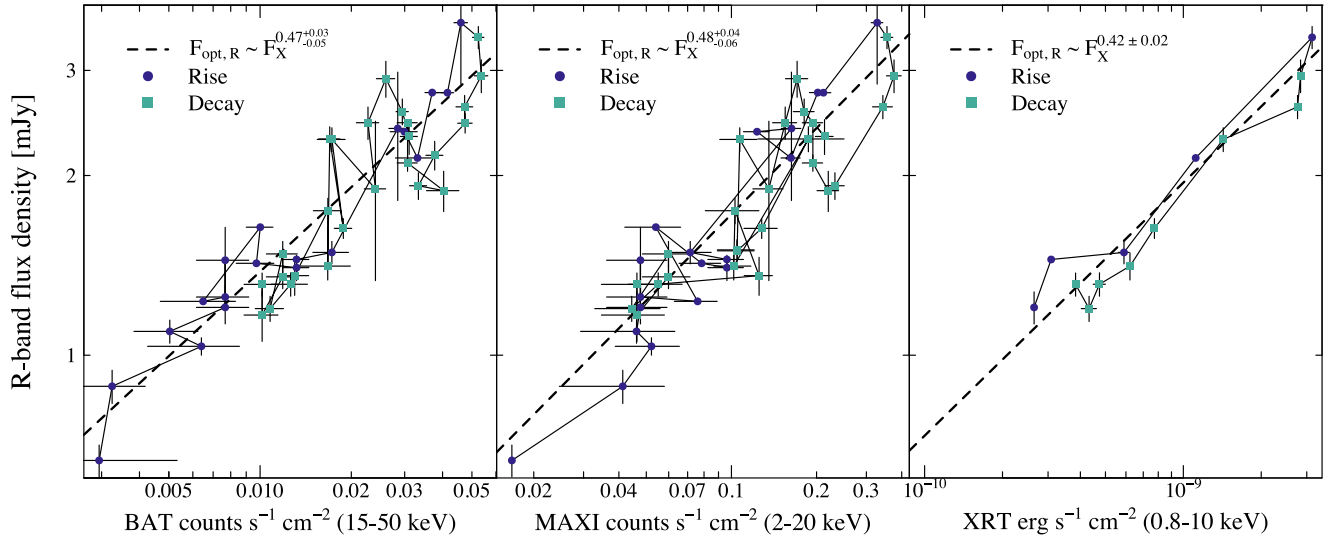
Figure 8. Optical/X-ray correlation. Left: optical *R*-band flux density as a function of the *Swift*/BAT flux density. The dashed line shows the best least-squares fit to the data, with the resulting slope marked in the legend on the upper left. The rise and decay parts of the outburst have been marked with different colours and symbols (blue circles for the rise and turquoise squares for the decay). Middle: same as in the left-hand panel but the optical *R*-band flux density is plotted as a function of MAXI flux density. Right: same as in the left-hand panel but the optical *R*-band flux density is plotted as a function of the 0.8–10 keV X-ray flux. Due to the requirement that the optical and X-ray observations should be within a day, the number of simultaneous *Swift* pointings with the optical is lower as compared to the monitoring data.
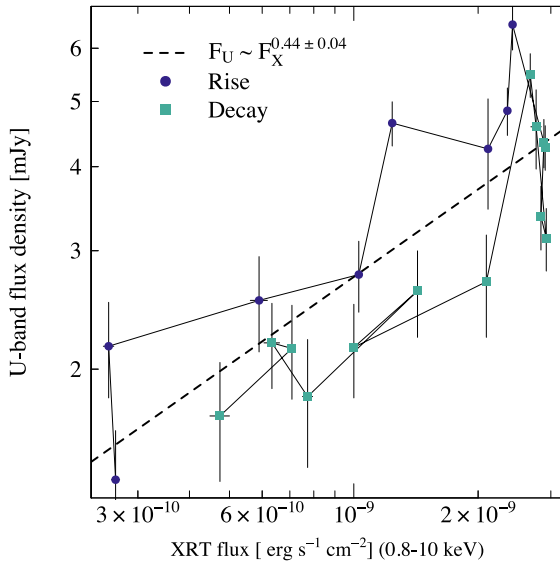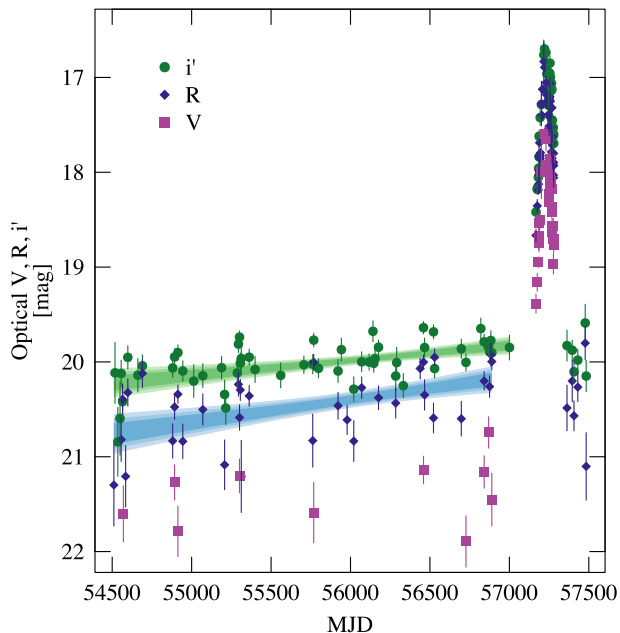
Figure 9. UV/X-ray correlation. Same as in Fig. 8, but *U*-band flux density as a function of the 0.8–10 keV X-ray flux.
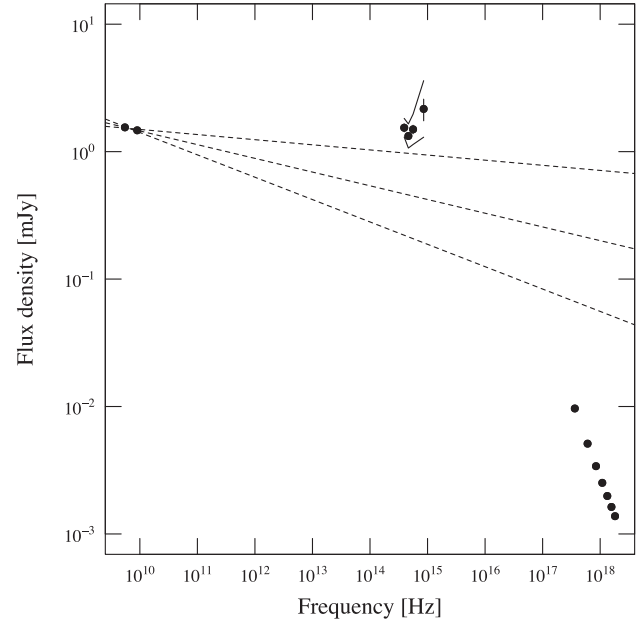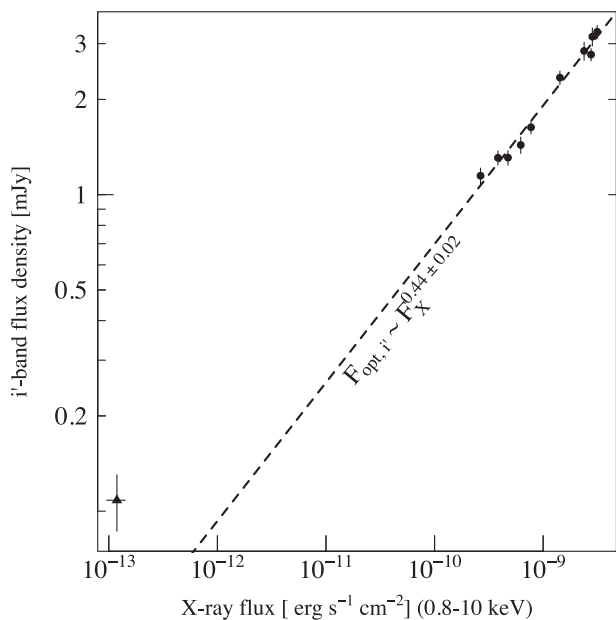
Figure 10. The multiwavelength SED of GS 1354−64. The dotted lines show the possible slopes of the power-law spectrum from synchrotron radiation based on the 1σ errors of the radio data points. The solid lines in the optical/UV frequencies show the range of the SED with varying values for A_V (2.6 ± 0.31). The *Swift*/XRT X-ray spectrum has a low count rate and thus it has been binned to seven bands from 1.5 to 7.5 keV for clarity.

subsequently increasing the X-ray brightness of the source. As the accretion disc pushes inwards into the hot accretion flow, it cools the corona by Compton scattering, which is seen as the softening of the X-ray spectra, but not enough to make the source transit to the soft state. This also happened in the 1997 outburst (Revnivtsev et al. 2000). Finally, the irradiation prevents the formation of a cooling front, and the disc is drained by viscous accretion of matter (King & Ritter 1998), which produces an exponential decay of the light curve, which is seen in the outburst decay of GS 1354−64. It is interesting to note that the index of the exponential rise/decay

changes during the outburst. This could arise from changes in the radiative efficiency as discussed in Eckersall, Vaughan & Wynn (2015). They found that a factor of ∼2 change in the decay time-scale is expected assuming a change from radiatively efficient

The Comptonized X-ray spectra show that there is little direct emission from the accretion disc. The seed photon temperature stays <0.4 keV, while in soft state LMXBs the temperature is usually ~1 keV. Therefore, the mass accretion rate does not become large enough for the disc to condensate from the optically thin accretion flow, which dominates the X-ray emission. Meyer-Hofmeister (2004) consider $L_X/L_{Edd} < 0.05$ as a requirement for the evaporation/condensation scheme to hold. Observationally, this limit can be as high as $L_X/L_{Edd} < 0.11$ (Tetarenko et al. 2016). For larger luminosities, the disc should approach the innermost stable orbit.

4.2 A 'high-hard' outburst

In Table 1, the average outburst peak unabsorbed 0.8–100 keV luminosity is 1.03×10^{-8} erg s^{-1} cm^{-2}. In Eddington units, this value can be presented as $L_X/L_{Edd} = 0.01\ d[\text{kpc}]^2/M_{BH}[\text{M}_\odot]$. For values of $d = 25$ kpc and $M_{BH} = 10$ M$_\odot$, the Eddington ratio is $L_X/L_{Edd} = 0.6$. A similar flux level was reached in the 1987 outburst, but this time the source was reported to have a soft state X-ray spectrum (the luminosity reported was $3.5 \times 10^{37}(d/10\ \text{kpc})$ erg s^{-1} in the energy band 1–10 keV; Kitamoto et al. 1990). Therefore, the current outburst was likely to have been on the brink of turning to a soft state. However, the critical luminosity for state transition is variable between individual sources, and even between individual outbursts of a same source (GX 339−4; e.g. Belloni et al. 2006). Tetarenko et al. (2016) found that the limiting Eddington ratio for hard-only outburst is $L_{Edd} < 0.11$. However, the peak luminosity of the 2015 outburst is several times brighter without the source transiting to the soft state. This might either indicate that this limit is higher or that the distance to GS 1354−64 is overestimated.

Extrapolating and integrating over the bolometric X-ray flux gives a rough estimate of the X-ray fluence of the outburst: 0.04 erg cm^{-2}, or 3×10^{45} erg for a distance of 25 kpc. With the standard efficiency of $\epsilon \sim 0.1$, this corresponds to 3×10^{25} g of matter accreted. If the accretion disc was emptied during both the previous and current outbursts, we can estimate the average mass accretion rate as 5×10^{16} g s^{-1} (or 8.5×10^{-10} M$_\odot$ yr^{-1}).

We can estimate an upper limit for the mass of the black hole given the mass ratio $q = 0.13 \pm 0.02$, and that the type of the companion star is G0 III–G5 III (Casares et al. 2004). A normal G0 III–G5 III star has typically mass in the range 2.1–2.4 M$_\odot$. However, due to mass-loss, the companion is likely a lower mass and more evolved star. Casares et al. (2004) estimate that the companion mass should be less than 2.1 M$_\odot$ based on the orbital period and the resulting estimate of the Roche lobe equivalent stellar radius, spectral classification and using the Stefan–Boltzmann relation. This results in the upper limit for the black hole mass of 16 ± 3 M$_\odot$, and subsequently for the Eddington luminosity of $L_X/L_{Edd} > 0.38^{+0.09}_{-0.06}$ for a distance of 25 kpc. Even for the minimum distance (15.6 kpc) as suggested by Reynolds & Miller (2011), the Eddington luminosity is greater than $0.15^{+0.04}_{-0.02}$.

A high Eddington luminosity is unusual for the canonical hard X-ray state. We rule out that GS 1354−64 would have been in a hard-intermediate state (HIMS) by its X-ray spectral and timing properties. The X-ray spectra are best fitted with a thermal Comptonization model, i.e. approximately a cut-off power law ($\Gamma = 1.2$–1.7), while in the HIMS the power law is steeper ($\Gamma > 2.1$) and usually without any cutoff. As the accretion disc is not statistically required in the fits to the *Swift* spectra, the accretion disc fraction has to be small and under values observed in the HIMS where the disc usually contributes to the spectra more than 20 per cent. The observed QPO frequencies are also very low suggesting a hard

Figure 11. Long-term light curves of the optical bands. The shaded, coloured regions show the 95, 99 and 99.9 per cent confidence intervals on the linear regression. The colour scheme is the same as in Fig. 1.

Figure 12. The optical i'-band flux density as a function of the 0.8–10 keV X-ray model flux with an additional data point from the quiescent state observed with *Chandra* (Reynolds & Miller 2011). The dashed line shows the best least-squares fit to the data, when excluding the quiescent data point. The quiescent data point lies well above the best-fitting line, and thus it is likely that the optical/X-ray relation turns to a shallower one in the quiescent state as compared to the outburst.

emission in the soft state to radiatively inefficient emission in the hard state. In the 2015 outburst, GS 1354−64 did not exhibit a state transition, but it has been suggested that some sources may change into a radiatively efficient accretion state in the hard state as well (e.g. H1743−322; Coriat et al. 2011).

state, while generally the QPO frequencies in the HIMS are higher (>1 Hz; Vignarca et al. 2003). Possible comparable sources to GS 1354−64 showing a luminous hard state are GRS 1915+105 and V404 Cyg. Since its discovery, GRS 1915+105 has been constantly found accreting at a high luminosity, including a state what could be categorized as a hard state ($L_X/L_{Edd} \sim 0.1$–0.4; Peris et al. 2016). However, due to the accretion disc being very hot in this source (>1 keV), the disc fraction is very high unless $L_X/L_{Edd} \sim 0.1$. In addition, the X-ray timing properties of GRS 1915+105 resemble more HIMS than hard state (Reig, Belloni & van der Klis 2003), and thus it is not clear if GRS 1915+105 displays the canonical hard X-ray state. V404 Cyg can produce hard outbursts that reach L_{Edd} (e.g. Życki, Done & Smith 1999; Rodriguez et al. 2015). Especially in the 1989 outburst, the spectral model is similar to the one fitted in this paper with low electron temperature and slightly higher optical depth ($kT_e \sim 10$ keV, $\tau \sim 6.5$; Życki et al. 1999), but the model to fit the spectra from June 2015 outburst is more complex with higher electron temperature ($kT_e \sim 40$ keV) and the seed photon temperature of the Comptonization being very high (∼7 keV; Natalucci et al. 2015). In any case, the overall outburst evolution of V404 Cyg is completely different compared to GS 1354−64, as V404 Cyg displays multiple flares, shows spectral variability in minute time-scales, probably because of variable absorption in the line of sight, and changes X-ray state during outburst and during individual flares (Życki et al. 1999; Rodriguez et al. 2015; Radhika et al. 2016). The energy spectra of V404 Cyg during an outburst are also markedly different from those of GS 1354−64, showing a strong (up to 0.6 L_{Edd}), un-Comptonized disc component (Życki et al. 1999; Radhika et al. 2016). Thus, it is not clear if V404 Cyg either displays the canonical hard X-ray state with a very high luminosity.

4.3 Optical/UV emission processes

After the outburst peak, the optical (*V* and *R* bands) drop more quickly compared to the X-ray and turn to an anticorrelation, reminiscent of the behaviour of other black hole transients when they switch to the soft X-ray state, e.g. XTE J1550−564 (Russell et al. 2007) and GX 339−4 (Coriat et al. 2009). In both cases, this was found to be associated with a change in optical colour, and was interpreted as due to the jet component increasing in the optical/IR after the soft-to-hard state transition. However, this is not the case in GS 1354−64, as the source is in the hard X-ray state during the whole outburst, and we do not have evidence for a change in the optical colour. After the optical drop, the relation turns to an anticorrelation because of periods of brightening in what seems to be a series of flares in the optical light curve. A counterpart to these flares is not seen in the X-ray light curves, and thus we can rule out the flares occurring in the optically thin accretion flow. Optical reflares have been suggested to arise from a sequence of heating and cooling front reflections in the accretion disc (Menou et al. 2000). If the optical reflare is produced in the accretion disc, it should produce a different correlation coefficient with the X-rays (0.3 as discussed in Section 3.5). Assuming that the quiescent state emission is dominated by the disc, this correlation should span the quiescent state value as well, which is the case as found in Section 3.5. However, the disc irradiation should inhibit the formation of cooling fronts (Dubus, Hameury & Lasota 2001), thus presenting doubts for this mechanism. Another possible mechanism could be flares in the jet, which would increase the synchrotron flux in the optical bands. From Fig. 3 (right-hand panel), we see that all the bands rise and decay in unison; thus, the jet contribution should be approximately equal in all bands, i.e. more or less a flat

spectrum (consistent with the radio spectral index −0.10 ± 0.05). The multiwavelength SED in Fig. 10 demonstrates that if the jet spectrum is continued to optical frequencies without a cutoff, it can present a sizeable contribution in the optical bands. Due to the scatter and larger error bars in the UV light curve, it is difficult to say whether the reflares are visible in the *U* band or not. However, without radio/IR coverage over the outburst, the jet contribution is difficult to ascertain.

In Section 3.3, the optical, UV and X-ray light curves were found to be correlated with $L_{opt/UV} \approx L_X^{0.4-0.5}$. This value is consistent with the X-ray irradiated accretion disc (van Paradijs & McClintock 1994) with a possible contribution from the viscous disc (Russell et al. 2006). Based on one multiwavelength SED (Fig. 10), the jet contribution cannot explain (if at all) the whole optical flux; thus, it is likely that the reprocessing contributes in the optical/UV frequencies. A similar value ($L_{opt} \approx L_X^{0.56}$) was obtained for V404 Cyg in the hard state during an outburst, which was resolved to be a combination of the contributions from the jet and reprocessing (Bernardini et al. 2016a), where the slightly higher correlation coefficient, as compared to GS 1354−64, could arise from a bigger jet contribution. In the case of GS 1354−64, it is possible that the optical/UV and their correlations with the X-ray are affected by the viscous disc. For viscous disc, the correlation coefficient is expected to get smaller with longer wavelengths and the correlation coefficient of optical/X-ray should be ∼0.3 (Russell et al. 2006), which are both not observed, but the contribution from the viscous disc could lower the correlation coefficient from the theoretical value of 0.5 for irradiation. In addition, as the UV/optical SEDs are flat during the outburst, this argues against the UV/optical originating from the Rayleigh–Jeans part of a blackbody spectrum. However, the SEDs could be also inverted for higher values of extinction, and thus conclusions cannot be made based on the optical/UV SEDs. Overall, it can be assumed that the during the outburst the emission from the irradiation is dominating with a smaller contribution from the viscous disc and perhaps a contribution from the jet if the jet break lies above optical/UV. In any case, the underlying scaling factor is the mass accretion rate, which drives the evolution in all bands.

4.4 Quiescent data

All versions of the DIM predict increasing quiescent fluxes (by as much as 1–2 mag), which is due to increasing surface density and effective temperature as matter accumulates to the disc. In contrast, the observations of dwarf nova outbursts have shown that the quiescent fluxes are constant or decreasing (Smak 2000). We have shown in Fig. 11 that a statistically significant rise is observed in the optical light curves. Assuming that the increase (0.56 mag in 2500 d in the *R* band) has been constant from the previous outburst (∼6500 d), the total optical brightening would have been ∼1.5 mag, consistent with the prediction of the DIM. According to the few *R*-band observations taken during a 10 yr period after the 1997 outburst as presented in Casares et al. (2009, their fig. 4), the *R*-band magnitude went down to 21.5 supporting the trend. However, this observation was taken about four years after the outburst, and two years after this observation the source displayed a much higher magnitude reaching up to 19.5, perhaps presenting an optical flare rising above the usual quiescence level. Thus, on top of the slow optical brightening and aperiodic, order-of-magnitude flaring, there is evidence of brighter flares during quiescence.

Recently, a similar linear, optical brightening ($\Delta V \sim 0.8$ mag) has been observed from Nova Muscae 1991 (Wu et al. 2016). Why

is this optical rise seen in GS 1354−64 and Nova Muscae 1991 but not in other sources? One possibility is that in GS 1354−64 there is evidence of the accretion flow dominating the optical flux even in quiescence from its large amplitude variability (Casares et al. 2009). This is not the case for sources like GRO J1655−40, where the star dominates the optical emission in quiescence (Greene, Bailyn & Orosz 2001). In many LMXBs, the star and the accretion flow can both be detected in quiescence: e.g. XTE J1118+480 (Gelino et al. 2006), A0620−00 (Cantrell et al. 2008) and V404 Cyg (Zurita et al. 2004). These LMXBs that have the accretion flow contributing or dominating to the optical emission in quiescence also show occasionally high amplitude variability during the quiescence similar to GS 1354−64 (Zurita et al. 2003, 2004; Hynes et al. 2009; Yang et al. 2012). Interestingly, in V404 Cyg, a several-years-long slow optical fade was followed by a low-amplitude, relatively fast rise of a few months prior to the June 2015 outburst when the contribution of the star was removed (Bernardini et al. 2016b). However, in some systems the accretion flow dominates with little or no evidence of the star making a contribution: e.g. GX 339−4 (Shahbaz, Fender & Charles 2001) and Swift J1357.2−0933 (Shahbaz et al. 2013; Mata Sánchez et al. 2015), but no long-term quiescent light curves exist for these sources. This may be the first time a slow years-time-scale optical rise has been seen from an X-ray binary together with an outburst. To determine whether this is a more ubiquitous phenomenon in XRBs, more long-term, continuous observations of LMXBs are needed.

GS 1354−64 is very X-ray bright in the quiescence ($L_X \gtrsim 10^{34}$ erg s^{-1} $\sim 10^{-5} L_{Edd}$; Reynolds & Miller 2011) as compared to other LMXBs ($\sim 10^{31}$ erg s^{-1}). This implies a mass accretion rate $\dot{M} = L_X / \epsilon c^2 \sim \epsilon^{-1} 10^{13}$ g s^{-1}. The efficiency, ϵ, varies in ADAF solutions depending on the mass accretion rate and the efficiency of electron heating, but generally lies in the region 0.001–0.05 (Yuan & Narayan 2014). Thus, the mass accretion rate in the quiescence state is 2×10^{14}–10^{16} g s^{-1} (or 10^{-4}–7×10^{-3} in Eddington accretion rates for a $10\,M_\odot$ black hole). These values are below the average mass accretion rate as obtained from the outburst energetics, and thus reasonable in the context of DIM. The range of values for the efficiency allow also accretion rate values that are less than the critical value of ADAF solutions ($\dot{M}_{crit,ADAF} \sim 10^{-3}$ for $\epsilon > 0.007$), and correspond to a scenario where the electrons radiate efficiently, but where the Coulomb collisions are still inefficient and thus the ions transfer only a small fraction of their energy to the electrons and remain advection dominated (Yuan & Narayan 2014). Thus, the quiescent data are consistent with the DIM including disc evaporation, where the inner accretion flow is of a bright ADAF type.

5 CONCLUSIONS

We have studied in detail the evolution of the 2015 outburst of GS 1354−64 in the optical, UV and X-ray frequencies. The outburst was found to stay in the hard X-ray state despite reaching ~ 60 per cent of the Eddington luminosity (for a distance of 25 kpc and $M_{BH} = 10\,M_\odot$), thus presenting us one of the best example of a hard, or 'failed', outburst with multiwavelength coverage throughout the outburst. We found that the optical emission, as well as the UV emission, is tightly correlated with the X-ray emission with a correlation coefficient of ~ 0.4–0.5, that is consistent with irradiation contributing to the optical/UV frequencies, with a smaller contribution from the viscous disc. The X-ray spectra can be fitted well with a Comptonization model, and show softening towards the end of the outburst. In addition, we detect a QPO in the

X-ray light curves with increasing centroid frequency during the peak and decay parts of the outburst. As discussed above, this behaviour could be explained by the DIM with irradiation and disc evaporation/condensation. Finally, we studied the long-term optical light curves and found a statistically significant, slow rise of the source brightness at optical frequencies during the quiescence state. We argue that this behaviour is the much-sought observational evidence of matter slowly accumulating in the accretion disc, and subsequently getting optically brighter, as predicted by the DIM. The reason why this is not observed in other sources is proposed to be the unusually bright accretion disc dominating the optical emission in the quiescent state of GS 1354−64.

REFERENCES

Balbus S. A., Hawley J. F., 1991, ApJ, 376, 214
Belloni T. M., 2010, in Belloni T., ed., Lecture Notes in Physics, Vol. 794, The Jet Paradigm. Springer-Verlag, Berlin, p. 53
Belloni T. et al., 2006, MNRAS, 367, 1113
Bernardini F., Russell D. M., Koljonen K. I. I., Stella F., Hynes R. I., Corbel S., 2016a, preprint (arXiv:1604.08022)
Bernardini F., Russell D. M., Shaw A. W., Lewis F., Charles P. A., Koljonen K. I. I., Lasota J. P., Casares J., 2016b, ApJ, 818, L5
Brocksopp C., Jonker P. G., Fender R. P., Groot P. J., van der Klis M., Tingay S. J., 2001, MNRAS, 323, 517
Brocksopp C., Bandyopadhyay R. M., Fender R. P., 2004, New Astron., 9, 249
Cadolle Bel M. et al., 2011, A&A, 534, A119
Cantrell A. G., Bailyn C. D., McClintock J. E., Orosz J. A., 2008, ApJ, 673, L159
Casares J., Zurita C., Shahbaz T., Charles P. A., Fender R. P., 2004, ApJ, 613, L133
Casares J. et al., 2009, ApJS, 181, 238
Chen W., Shrader C. R., Livio M., 1997, ApJ, 491, 312
Coriat M., Corbel S., Buxton M. M., Bailyn C. D., Tomsick J. A., Körding E., Kalemci E., 2009, MNRAS, 400, 123
Coriat M. et al., 2011, MNRAS, 414, 677
Coriat M., Tzioumis T., Corbel S., Fender R., Miller-Jones J., 2015, Astron. Telegram, 7656, 1
Curran P. A., 2014, preprint (arXiv:1411.3816)
Dubus G., Lasota J.-P., Hameury J.-M., Charles P., 1999, MNRAS, 303, 139
Dubus G., Hameury J.-M., Lasota J.-P., 2001, A&A, 373, 251
Eckersall A. J., Vaughan S., Wynn G. A., 2015, MNRAS, 450, 3410

Fitzpatrick E. L., 1999, PASP, 111, 63

Francey R. J., 1971, Nat. Phys. Sci., 229, 229

Frank J., King A., Raine D. J., 2002, Accretion Power in Astrophysics, 3rd edn. Cambridge Univ. Press, Cambridge

Gelino D. M., Balman Ş., Kızıloğlu Ü., Yılmaz A., Kalemci E., Tomsick J. A., 2006, ApJ, 642, 438

Greene J., Bailyn C. D., Orosz J. A., 2001, ApJ, 554, 1290

Güver T., Özel F., 2009, MNRAS, 400, 2050

Houck J. C., Denicola L. A., 2000, in Manset N., Veillet C., Crabtree D., eds, ASP Conf. Ser. Vol. 216, Astronomical Data Analysis Software and Systems IX. Astron. Soc. Pac., San Francisco, p. 591

Hynes R. I., Mauche C. W., Haswell C. A., Shrader C. R., Cui W., Chaty S., 2000, ApJ, 539, L37

Hynes R. I., Bradley C. K., Rupen M., Gallo E., Fender R. P., Casares J., Zurita C., 2009, MNRAS, 399, 2239

Kalberla P. M. W., Burton W. B., Hartmann D., Arnal E. M., Bajaja E., Morras R., Pöppel W. G. L., 2005, A&A, 440, 775

King A. R., Ritter H., 1998, MNRAS, 293, L42

Kitamoto S., Tsunemi H., Pedersen H., Ilovaisky S. A., van der Klis M., 1990, ApJ, 361, 590

Koljonen K. I. I., Russell D. M., Lewis F., 2015, Astron. Telegram, 7887, 1

Krimm H. A. et al., 2013, ApJS, 209, 14

Lasota J.-P., 2001, New Astron. Rev., 45, 449

Lewis F., Russell D. M., Fender R. P., Roche P., Clark J. S., 2008, Proc. Sci., Microquasars and Beyond. SISSA, Trieste, PoS(MQW7)069

Maccarone T. J., Coppi P. S., 2003, MNRAS, 338, 189

Makino F., 1987, IAU Circ., 4342, 1

Markert T. H., Canizares C. R., Clark G. W., Hearn D. R., Li F. K., Sprott G. F., Winkler P. F., 1977, ApJ, 218, 801

Markert T. H. et al., 1979, ApJS, 39, 573

Markoff S., Falcke H., Fender R., 2001, A&A, 372, L25

Mata Sánchez D., Muñoz-Darias T., Casares J., Corral-Santana J. M., Shahbaz T., 2015, MNRAS, 454, 2199

Matsuoka M. et al., 2009, PASJ, 61, 999

Menou K., Hameury J.-M., Lasota J.-P., Narayan R., 2000, MNRAS, 314, 498

Merloni A., Di Matteo T., Fabian A. C., 2000, MNRAS, 318, L15

Meyer-Hofmeister E., 2004, A&A, 423, 321

Natalucci L., Fiocchi M., Bazzano A., Ubertini P., Roques J.-P., Jourdain E., 2015, ApJ, 813, L21

Naylor T., 1998, MNRAS, 296, 339

Peris C. S., Remillard R. A., Steiner J. F., Vrtilek S. D., Varniere P., Rodriguez J., Pooley G., 2016, ApJ, 822, 60

Radhika D., Nandi A., Agrawal V. K., Mandal S., 2016, preprint (arXiv:1601.03234)

Reig P., Belloni T., van der Klis M., 2003, A&A, 412, 229

Revnivtsev M. G., Borozdin K. N., Priedhorsky W. C., Vikhlinin A., 2000, ApJ, 530, 955

Reynolds M. T., Miller J. M., 2011, ApJ, 734, L17

Reynolds M. T., Reis R. C., Miller J. M., Cackett E. M., Degenaar N., 2014, MNRAS, 441, 3656

Rodriguez J. et al., 2015, A&A, 581, L9

Russell D. M., Lewis F., 2015, Astron. Telegram, 7637, 1

Russell D. M., Fender R. P., Hynes R. I., Brocksopp C., Homan J., Jonker P. G., Buxton M. M., 2006, MNRAS, 371, 1334

Russell D. M., Maccarone T. J., Körding E. G., Homan J., 2007, MNRAS, 379, 1401

Russell D. M., Maitra D., Dunn R. J. H., Markoff S., 2010, MNRAS, 405, 1759

Russell D. M. et al., 2013, MNRAS, 429, 815

Shahbaz T., Fender R., Charles P. A., 2001, A&A, 376, L17

Shahbaz T., Dhillon V. S., Marsh T. R., Zurita C., Haswell C. A., Charles P. A., Hynes R. I., Casares J., 2003, MNRAS, 346, 1116

Shahbaz T., Russell D. M., Zurita C., Casares J., Corral-Santana J. M., Dhillon V. S., Marsh T. R., 2013, MNRAS, 434, 2696

Shakura N. I., Sunyaev R. A., 1973, A&A, 24, 337

Smak J., 2000, New Astron. Rev., 44, 171

Stetson P. B., 1987, PASP, 99, 191

Tetarenko B. E., Sivakoff G. R., Heinke C. O., Gladstone J. C., 2016, ApJS, 222, 15

Titarchuk L., 1994, ApJ, 434, 570

van Paradijs J., McClintock J. E., 1994, A&A, 290, 133

Veledina A., Poutanen J., Vurm I., 2013, MNRAS, 430, 3196

Vignarca F., Migliari S., Belloni T., Psaltis D., van der Klis M., 2003, A&A, 397, 729

Wu J., Orosz J. A., McClintock J. E., Hasan I., Bailyn C. D., Gou L., Chen Z., 2016, preprint (arXiv:1601.00616)

Yang Y. J., Kong A. K. H., Russell D. M., Lewis F., Wijnands R., 2012, MNRAS, 427, 2876

Yuan F., Narayan R., 2014, ARA&A, 52, 529

Yuan F., Quataert E., Narayan R., 2003, ApJ, 598, 301

Zurita C., Casares J., Shahbaz T., 2003, ApJ, 582, 369

Zurita C., Casares J., Hynes R. I., Shahbaz T., Charles P. A., Pavlenko E. P., 2004, MNRAS, 352, 877

Życki P. T., Done C., Smith D. A., 1999, MNRAS, 309, 561

SUPPORTING INFORMATION

Additional Supporting Information may be found in the online version of this article:

Table A1. Optical monitoring data from Faulkes/LCOGT *i′* band.
Table A2. Optical monitoring data from Faulkes/LCOGT *R* band.
Table A3. Optical monitoring data from Faulkes/LCOGT *V* band.
Table A4. Optical monitoring data from LCOGT *B* band.
Table A5. Optical monitoring data from SMARTS *R* band.
(http://www.mnras.oxfordjournals.org/lookup/suppl/doi:10.1093/mnras/stw1007/-/DC1).

Please note: Oxford University Press is not responsible for the content or functionality of any supporting materials supplied by the authors. Any queries (other than missing material) should be directed to the corresponding author for the article.

APPENDIX A: OPTICAL MONITORING DATA FROM FAULKES/LCOGT AND SMARTS

Table A1. Optical monitoring data from Faulkes/LCOGT i' band. FTS = Faulkes Telescope South; L[X] = LCOGT, with [X] denoting the telescope number. Note: Full table is available online.

MJD	i' (mag)	Err (mag)	Tel	MJD	i' (mag)	Err (mag)	Tel	MJD	i' (mag)	Err (mag)	Tel
54517.623	20.11	0.32	FTS	56070.377	20.00	0.11	FTS	57221.137	16.70	0.05	L5
54535.433	20.84	0.36	FTS	56117.367	20.00	0.09	FTS	57230.452	16.74	0.07	L11
54549.427	20.59	0.39	FTS	56141.454	19.68	0.11	FTS	57234.390	16.88	0.05	L11
⋮	⋮	⋮	⋮	⋮	⋮	⋮	⋮	⋮	⋮	⋮	⋮

Table A2. Optical monitoring data from Faulkes/LCOGT R band. FTS = Faulkes Telescope South; L[X] = LCOGT, with [X] denoting the telescope number. Note: Full table is available online.

MJD	i' (mag)	Err (mag)	Tel	MJD	i' (mag)	Err (mag)	Tel	MJD	i' (mag)	Err (mag)	Tel
54510.546	21.30	0.43	FTS	56459.472	20.00	0.07	FTS	57253.368	17.42	0.03	L11
54556.440	20.82	0.23	FTS	56466.397	20.35	0.16	FTS	57253.741	17.31	0.07	L13
54565.424	20.39	0.15	FTS	56522.422	20.59	0.16	FTS	57254.749	17.20	0.05	L12
⋮	⋮	⋮	⋮	⋮	⋮	⋮	⋮	⋮	⋮	⋮	⋮

Table A3. Optical monitoring data from Faulkes/LCOGT V band. FTS = Faulkes Telescope South; L[X] = LCOGT, with [X] denoting the telescope number. Note: Full table is available online.

MJD	i' (mag)	Err (mag)	Tel	MJD	i' (mag)	Err (mag)	Tel	MJD	i' (mag)	Err (mag)	Tel
54570.406	21.60	0.30	FTS	57186.582	18.69	0.15	L3	57254.747	18.03	0.08	L12
54892.672	21.27	0.19	FTS	57187.008	18.67	0.07	L5	57255.714	17.86	0.11	L10
54913.691	21.79	0.27	FTS	57193.695	18.51	0.09	L13	57258.388	18.10	0.10	L3
⋮	⋮	⋮	⋮	⋮	⋮	⋮	⋮	⋮	⋮	⋮	⋮

Table A4. Optical monitoring data from LCOGT B band. L[X] = LCOGT, with [X] denoting the telescope number. Note: Full table is available online.

MJD	i' (mag)	Err (mag)	Tel
57221.145	18.64	0.07	L5
57234.397	18.97	0.17	L11
57235.728	18.83	0.09	L12
⋮	⋮	⋮	⋮

Table A5. Optical monitoring data from SMARTS R band. Note: Full table is available online.

MJD	i' (mag)	Err (mag)
57188.995	18.00	0.01
57190.020	17.69	0.01
57192.004	17.84	0.01
⋮	⋮	⋮

This paper has been typeset from a TEX/LATEX file prepared by the author.